Available online at www.sciencedirect.com
ScienceDirect
International Journal of Heat and Fluid Flow 29 (2008) 640–653
International Journal of HEAT AND FLUID FLOW
www.elsevier.com/locate/ijhff

Application of a local SGS model based on coherent structures to complex geometries

H. Kobayashi [a,b,*], F. Ham [a], X. Wu [a,c]

[a] Center for Turbulence Research, Stanford University, Stanford, CA 94305-3035, USA
[b] Department of Physics, Keio University, 4-1-1, Hiyoshi, Kohoku-ku, Yokohama 223-8521, Japan
[c] Royal Military College of Canada, Kingston, Ontario, Canada K7K 7B4

Received 31 October 2007; received in revised form 13 February 2008; accepted 14 February 2008
Available online 1 April 2008

Abstract

A coherent structure model (CSM) as a subgrid-scale (SGS) model [Kobayashi, H., 2005. The subgrid-scale models based on coherent structures for rotating homogeneous turbulence and turbulent channel flow. Phys. Fluids 17, 045104] is applied to complex geometries and is assessed its performance in large-eddy simulation. The CSM is one of the local SGS models, which mean herein "no averaging in homogeneous directions". Two types of simulation code are tested for the assessment: a structured-mesh code is used for a flow over a backward-facing step, and an unstructured-mesh one is used for a flow in an asymmetric plane diffuser and for staggered jets in crossflow. For all configurations, the CSM gives good predictions and is almost the same performance as the dynamic models. This local model is simple and stable, and suitable for complex geometries.

PACS: 47.27.−i; 47.27.De; 47.27.E−; 47.27.ep

Keywords: Large-eddy simulation; Coherent structure; Subgrid-scale modeling; Complex geometry

1. Introduction

Coherent structures naturally arise in many turbulent flows, and coherent eddies are an important feature of turbulence. The existence of the coherent structures was verified by the direct numerical simulation (DNS). Vincent and Meneguzzi (1991) and Jiménez et al. (1993) visualized many vortex tubes with vorticity vectors in a homogeneous isotropic turbulence, and showed that the distribution of velocity derivative is strongly non-Gaussian.

Hunt et al. (1988) and Chong et al. (1990) classified the coherent structures using the second and the third invariants of a velocity gradient tensor. A positive second invariant indicates a coherent eddy whose vorticity is stronger than its strain. This definition of the positive second invariant is common to extract the coherent eddies, although there are lots of strict definitions or rigorous thresholds: for example, a criterion with a negative and the second largest eigenvalue of the second invariant (Jeong and Hussain, 1995) and a swirling strength criterion (Zhou et al., 1999; Chakraborty et al., 2005).

These coherent eddies scale with the Kolmogorov microscale and the rms of the velocity fluctuation, and have been found universally in homogeneous isotropic turbulence, planar channel flow, and mixing layers using direct numerical simulation (Miyauchi and Tanahashi, 2001). The most expected diameter of the coherent fine scale eddies is 10 times of the Kolmogorov microscale. Kida and Ohkitani (1992) showed that the high energy dissipation region has a double-peak structure and distributes

* Corresponding author. Address: Department of Physics, Keio University, 4-1-1, Hiyoshi, Kohoku-ku, Yokohama 223-8521, Japan. Tel./fax: +81 45 566 1323.
E-mail address: hkobayas@phys-h.keio.ac.jp (H. Kobayashi).

0142-727X/$ - see front matter © 2008 Elsevier Inc. All rights reserved.
doi:10.1016/j.ijheatfluidflow.2008.02.008

around the vortex tube. In a homogeneous isotropic turbulence and a temporally developing turbulent mixing layer, Tanahashi et al. (1996, 1997) also showed that the central region of a coherent fine scale eddy with a positive large second invariant gives a minimal energy dissipation, while the double-peak structure with a negative second invariant distributes in the surrounding region of the positive second invariant and gives maximal energy dissipations.

From the viewpoint of large-eddy simulation (LES), Da Silva and Métais (2002) used DNS data and showed the influence of the coherent structures on grid/subgrid-scale (GS/SGS) interactions in free shear layers. The most intense kinetic energy exchanges between GS and SGS occur near the coherent structures. However, GS/SGS transfer is not very well correlated with the coherent vortices. The so-called "local equilibrium assumption" holds globally but not locally because most viscous dissipation of SGS kinetic energy takes place within the vortex cores, whereas forward and backward GS/SGS transfer occurs at quite different locations.

Natrajan and Christensen (2006) investigated the relationship between SGS dissipation and embedded coherent structures within the log layer of wall turbulence using an ensemble of filtered GS velocity fields obtained from particle-image velocimetry. It was revealed that strong forward- and backward-scatter events occur spatially coincident to individual hairpin vortices and their larger-scale organization into vortex packets. The large-scale regions of forward scatter are observed along the inclined interface of the packets, coincident with strong ejections induced by the individual vortices. Strong backward-scatter of energy is observed at the trailing edge of the vortex packets and weaker backscatter is also noted locally around the individual heads of the hairpin structures. In LES, local SGS models, which mean herein "no averaging in homogeneous directions" to determine the model parameter, have been proposed, and the most famous local SGS model is Smagorinsky model (SM) (Smagorinsky, 1963). As well known, the model parameter changes among a homogeneous isotropic turbulence, a turbulent mixing layer, and a turbulent channel flow owing to a Reynolds number dependence of the parameter, so that a wall function is needed to damp its SGS eddy viscosity in the turbulent channel flow (see e.g., Rogallo and Moin, 1984, 1996).

This problem was resolved by Germano et al. (1991) using a dynamic procedure to determine the model parameter. This model is called the dynamic Smagorinsky model (DSM). It is no doubt that this procedure is the most important breakthrough in LES. However, averaging in homogeneous directions to determine the model parameter is needed to avoid a negative SGS eddy viscosity, which causes a numerical instability. This constraint makes it difficult to apply to complex geometries.

To resolve the constraint of averaging in the DSM, Ghosal et al. (1995) proposed a dynamic localization model (LDSM), in which the mathematical inconsistency of the model parameter in test-scale components equated with that in grid-scale components is improved. As a result, the flow over a backward-facing step can be stably carried out with locally determined model parameters. However, clipping operation is needed to avoid the negative SGS eddy viscosity. Meneveau et al. (1996) proposed a Lagrangian averaging along a pathline for the dynamic model. These improvements, however, need more CPU time in comparison with the DSM.

For engineering applications, some local SGS models have been proposed. These models have in common that the turbulent eddy viscosity is locally determined with fixed model-parameters. Nicoud and Ducros (1999) proposed a wall-adapting local eddy viscosity (WALE) model based on a tensor invariant with the proper scaling at the wall, and reproduced a transition in a periodic turbulent pipe flow. Yoshizawa et al. (2000) proposed a nonequilibrium fixed-parameter SGS model obeying the near-wall asymptotic constraint, and showed that the better performance than the SM is obtained for turbulent channel flows. Inagaki et al. (2002) suggested a mixed-time-scale SGS model with fixed model-parameters without an explicit wall-damping function for practical LES, and showed that it works better than the DSM and similar to the SM for the turbulent channel flows and the flow over a backward-facing step. Vreman (2004) proposed a SGS eddy viscosity model based on an algebraic theory only with the local filter width and the first-order derivatives of velocity field for turbulent shear flows, and showed that the model is more accurate than the SM as well as the DSM for a transitional and turbulent mixing layer and a turbulent channel flow. Shimomura (1994, 1995) suggested a SGS algebraic stress model and the model showed much better performance than the SM for homogeneous turbulences in a rotating frame.

Kobayashi (2005) proposed a coherent structure model (CSM) based on the coherent structures. The model parameter is composed of a fixed model-parameter and a coherent structure function, which is the second invariant in GS flow fields normalized by the magnitude of a velocity gradient tensor and plays a role of wall-damping. The CSM has been tested in a series of canonical turbulent flows including rotating and non-rotating channel flows and was found to yield a level of accuracy similar to that obtained by using the DSM. Moreover, the CSM gave a better prediction of relaminarization than the DSM and the SM for turbulent channel flows with a uniform magnetic field perpendicular to insulated walls (Kobayashi, 2006). The better performance was indicated in MHD turbulent duct flows. (Kobayashi, 2008).

In this study, the applicability of the CSM is further assessed in the simulations of a flow over a backward-facing step, a flow in an asymmetric plane diffuser, and staggered jets in crossflow. The performance of the CSM is compared to the DSM and the LDSM.

2. Numerical methods and SGS models

2.1. Numerical methods

The governing equations in this study are incompressible continuity and momentum equations; these equations are filtered for LES. We used a structured and an unstructured flow solvers developed at the Center for Turbulence Research, Stanford University.

The structured-mesh flow solver is called JETCODE (CHUCK'S CODE) and is adopted for a backward-facing step flow. This solver is based on a second-order central-discretization on a staggered-grid, a second-order time-advancement, and a Poisson equation for pressure solved using a multi-grid method (see Akselvoll and Moin, 1995, 2001).

The unstructured-mesh flow solver is named CDP after the late Dr. Charles David Pierce of the Center for Turbulence Research, Stanford University. This solver is used for a diffuser and a crossflow. The filtered continuity and momentum equations are solved on a cell-centered unstructured-mesh with a second-order accurate central difference spatial discretization. A fractional step method is used for a time-advancement procedure, and an implicit second-order Crank–Nicolson scheme is used for both convection and viscous terms. The Poisson equation is solved to determine the pressure field. For further details about the numerical algorithm, see Ham and Iaccarino (2004) and Mahesh et al. (2004).

2.2. SGS models

In LES, the SGS stress tensor $\tau_{ij} = \overline{u_i u_j} - \bar{u}_i \bar{u}_j$ is modeled. The DSM, the LDSM, and the CSM are examined in the present study.

2.2.1. Dynamic Smagorinsky model

In the DSM, τ^a_{ij} is modeled with the filter width $\overline{\Delta}$ as

$$\tau^a_{ij} = -2C\overline{\Delta}^2|\overline{S}|\overline{S}_{ij}, \tag{1}$$

where τ^a_{ij} is the traceless SGS stress tensor and is defined with the SGS stress tensor τ_{ij} by

$$\tau^a_{ij} = \tau_{ij} - \frac{1}{3}\tau_{aa}\delta_{ij}. \tag{2}$$

Here the velocity–strain tensor for the GS or resolved component $\overline{S}_{ij}$ and its magnitude $|\overline{S}|$ are defined by

$$\overline{S}_{ij} = \frac{1}{2}\left(\frac{\partial \bar{u}_j}{\partial x_i} + \frac{\partial \bar{u}_i}{\partial x_j}\right), \tag{3}$$

$$|\overline{S}| = \left(2\overline{S}_{ij}\overline{S}_{ij}\right)^{1/2}. \tag{4}$$

The model parameter of the DSM (Germano et al., 1991) is determined using a least square procedure proposed by Lilly (1992) with an average in homogeneous directions.

$$C = \frac{\langle L_{ij}M_{ij}\rangle}{\langle M_{ij}M_{ij}\rangle}, \tag{5}$$

where L_{ij} and M_{ij} are given by

$$L_{ij} = \widehat{\bar{u}_i\bar{u}_j} - \hat{\bar{u}}_i\hat{\bar{u}}_j, \tag{6}$$

$$M_{ij} = 2\overline{\Delta}^2\widehat{|\overline{S}|\overline{S}_{ij}} - 2\widehat{\overline{\Delta}}^2|\hat{\overline{S}}|\hat{\overline{S}}_{ij}, \tag{7}$$

where the double filter width $\widehat{\overline{\Delta}}$ is defined as

$$\frac{\widehat{\overline{\Delta}}}{\overline{\Delta}} = 2. \tag{8}$$

In this way, C is dynamically determined in the DSM. To compare the model parameters, the Smagorinsky constant $C_S = |C|^{1/2}$ is used hereafter. The test-filtered velocity $\widehat{\bar{u}_i}$ in homogeneous directions is calculated using a Simpson rule as

$$\hat{\bar{f}}_i = \frac{1}{6}\left(\bar{f}_{i-1} + 4\bar{f}_i + \bar{f}_{i+1}\right). \tag{9}$$

In (5), $\langle\ \rangle$ denotes the averaging in homogeneous directions. The averaging and the clipping under $\nu + \nu_t < 0$ (ν the molecular viscosity; ν_t the SGS eddy viscosity) is conducted to avoid any negative values.

This model is implemented to the simulations of a backward-facing step flow and a diffuser flow. Note that for the backward-facing step flow the filter width $\overline{\Delta} = (\overline{\Delta}_x\overline{\Delta}_z)^{1/2}$ is used instead of $\overline{\Delta} = (\overline{\Delta}_x\overline{\Delta}_y\overline{\Delta}_z)^{1/3}$ because a filtering in the y-direction is not adopted.

2.2.2. Dynamic localization model

The previous dynamic model needs at least one homogeneous direction to average the model parameter and to avoid its negative value. This restriction causes a difficulty when the model is applied to complex geometries.

Ghosal et al. (1995) resolved this problem using a variational formulation to dynamically determine the model parameter of the Smagorinsky model. The new formulation leads to an integral equation. This model is called the dynamic localization model and is referred as the LDSM in this study.

The LDSM is applicable to inhomogeneous flows and it does not suffer from the restriction of any homogeneous directions. However, this procedure requires an additional computational overhead to obtain the iterative solution of the integral equation. In addition, clipping operation is needed to avoid the negative eddy viscosity. The description of the procedure in detail is far beyond the extent of this paper, see more detail Ghosal et al. (1995).

2.2.3. Coherent structure model

There is two pathways to use the coherent structures for the SGS model: one is to reflect precisely spatial location between the coherent structures and the budget of the SGS kinetic energy, the other is to reflect the collective information about the budget to the SGS model. The for-

mer position is attractive, but it remains in the future study. The present model takes the latter position.

This is due to the selection of the SGS eddy viscosity model – actually Smagorinsky type model – in order to stably apply to complex geometries. In addition, the SGS eddy viscosity model is not well correlated with the true SGS stress tensor obtained from filtered DNS, whereas the SGS energy transfer – in another word the SGS energy dissipation – is well correlated with that obtained from filtered DNS (see e.g., Salvetti and Banerjee, 1995). Yet, the SGS eddy viscosity model cannot express the backward transfer. Again, the main objective in the present study is to stably apply the SGS model to complex geometries and to obtain reasonable results.

In the CSM (Kobayashi, 2005), the model parameter is "locally" defined as

$$C = C_{\mathrm{CSM}} |F_{\mathrm{CS}}|^{3/2} F_{\Omega}, \tag{10}$$

with

$$C_{\mathrm{CSM}} = \frac{1}{22}, \quad F_{\mathrm{CS}} = \frac{Q}{E}, \quad F_{\Omega} = 1 - F_{\mathrm{CS}}, \tag{11}$$

$$Q = \frac{1}{2}\left(\overline{W}_{ij}\overline{W}_{ij} - \overline{S}_{ij}\overline{S}_{ij}\right) = -\frac{1}{2}\frac{\partial \bar{u}_j}{\partial x_i}\frac{\partial \bar{u}_i}{\partial x_j}, \tag{12}$$

$$E = \frac{1}{2}\left(\overline{W}_{ij}\overline{W}_{ij} + \overline{S}_{ij}\overline{S}_{ij}\right) = \frac{1}{2}\left(\frac{\partial \bar{u}_j}{\partial x_i}\right)^2, \tag{13}$$

$$\overline{W}_{ij} = \frac{1}{2}\left(\frac{\partial \bar{u}_j}{\partial x_i} - \frac{\partial \bar{u}_i}{\partial x_j}\right), \tag{14}$$

where C_{CSM} is a fixed model constant, F_{CS} is the coherent structure function defined as the second invariant normalized by the magnitude of a velocity gradient tensor E, F_{Ω} is the energy-decay suppression function which becomes about 1.1 in homogeneous isotropic turbulences and at the center of turbulent channel flows, and $\overline{W}_{ij}$ is the vorticity tensor in a resolved flow field. Moreover, F_{CS} and F_{Ω} have definite upper and lower limits:

$$-1 \leqslant F_{\mathrm{CS}} \leqslant 1, \quad 0 \leqslant F_{\Omega} \leqslant 2. \tag{15}$$

As a result, the CSM has smaller variance of the model parameter than the DSM without averaging and the numerical simulation with the CSM is stably carried out even though the model parameter is locally determined (Kobayashi, 2005).

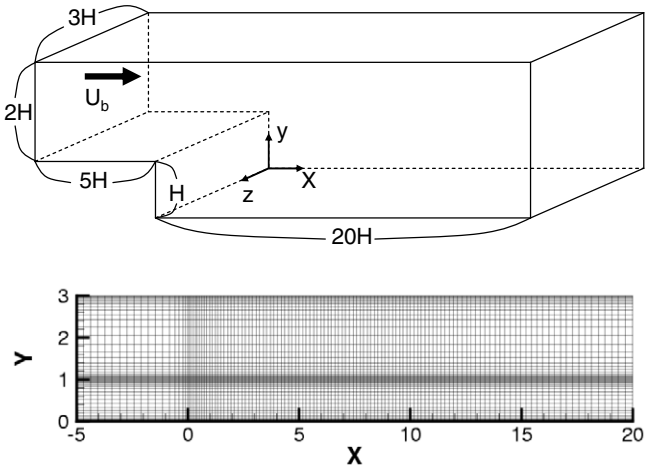

Fig. 1. Computational domain for a backward-facing step.

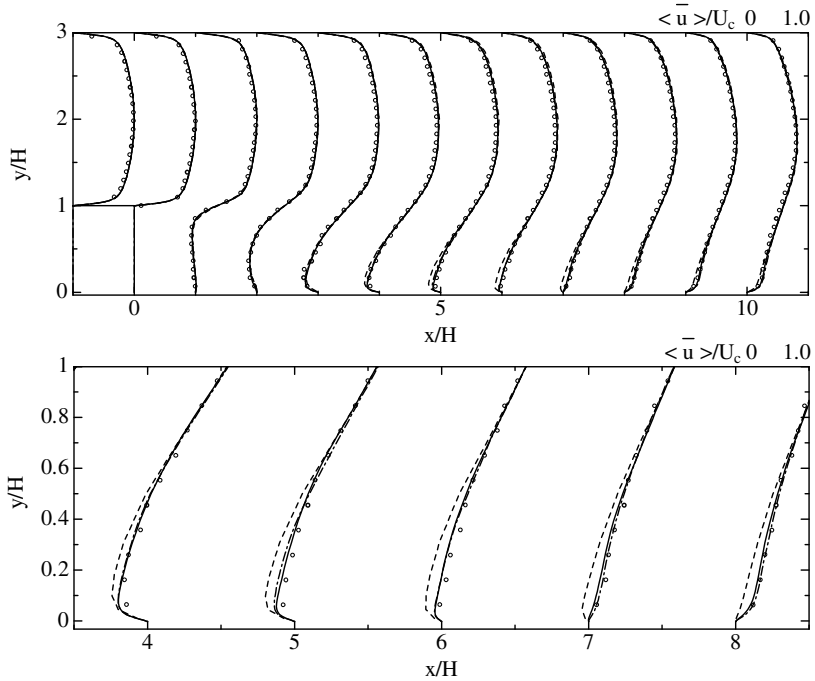

Fig. 2. Streamwise mean velocity profiles; (upper figure): inlet $\leqslant x/H \leqslant 10$, $0 \leqslant y/H \leqslant 3$; (lower figure): $4 \leqslant x/H \leqslant 8$, $0 \leqslant y/H \leqslant 1$. —, CSM; –·–, DSM; ----, no model; ○, experimental data by Kasagi and Matsunaga (1995).

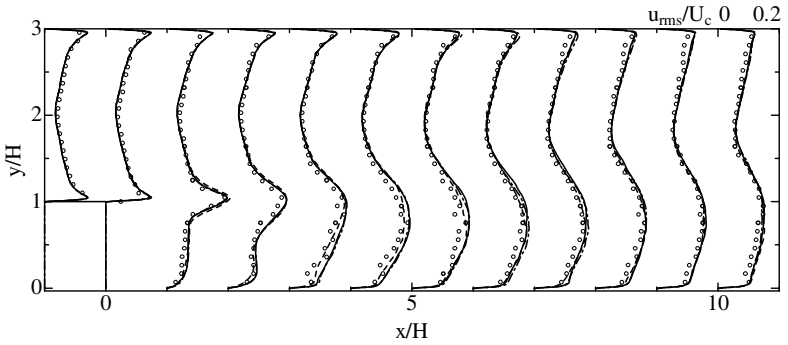

Fig. 3. Streamwise rms velocity profiles. —, CSM; –·–, DSM; ----, no model; ○, experimental data by Kasagi and Matsunaga (1995).

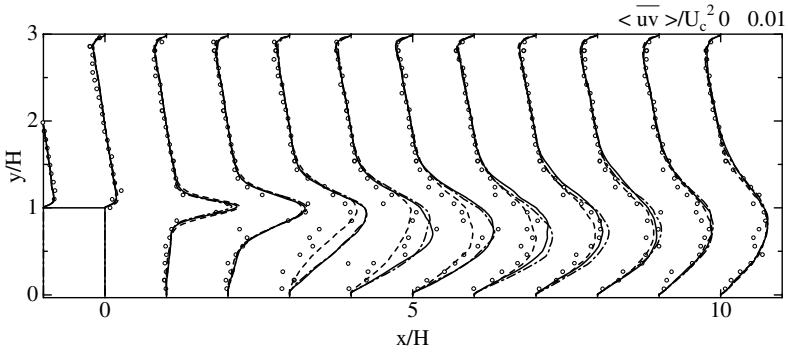

Fig. 4. Reynolds shear stress profiles. —, CSM; –·–, DSM; ----, no model; ○, experimental data by Kasagi and Matsunaga (1995).

3. Results and discussion

3.1. Backward-facing step flow

Fig. 1 shows the computational domain for a turbulent flow over a backward-facing step. The grid resolution is $256 \times 96 \times 64$ in the x, y, and z directions, respectively; x is the streamwise direction, y is the one normal to the walls, and z is the spanwise one. The Reynolds number based on the step height H and bulk velocity U_b was 4800. This value is close to 4775 in the experiment by Kasagi and Matsunaga (1995); the Reynolds number based on the step height and a centerline velocity at the inlet U_c is 5500. The domain depth in z-direction is $3H$. The grid was stretched out with the factors; 4 ($x/H = -5$): 4 ($x/H = -1$): 1 ($x/H = 0$): 2 ($x/H = 2$): 2 ($x/H = 10$): 4 ($x/H = 20$) in the x-direction; 1 ($y/H = 0$): 10 ($y/H = 0.5$): 1 ($y/H = 1$): 20 ($y/H = 2$): 1 ($y/H = 3$) in the y-direction. An inflow condition is imposed at $x/H = -5$, and the unsteady inflow profile is given a fully developed channel flow at $Re_\tau = 290$. The time step is $0.01H/U_b$. A convective condition is applied at the outflow boundary. Statistics for the CSM, the DSM, and no model are accumulated over 20,000 time steps ($200h/U_b$ time units), respectively. This simulation was

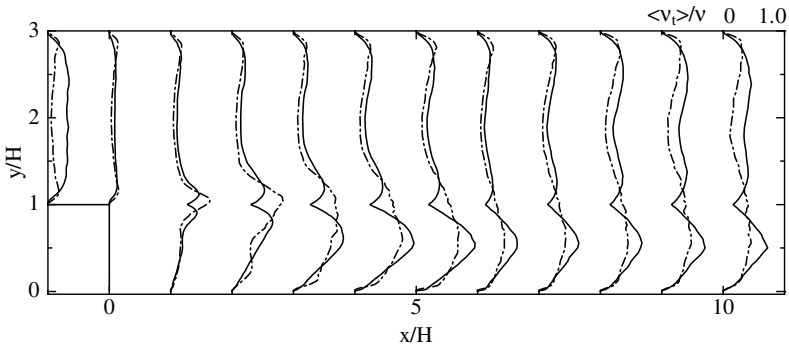

Fig. 5. Ratios of the SGS eddy viscosity and the molecular viscosity. —, CSM; –·–, DSM.

performed using JETCODE (CHUCK'S CODE), a structured incompressible flow solver developed at the Center for Turbulence Research, Stanford University (see Akselvoll and Moin, 1995, 2001).

Fig. 2 shows the profiles of streamwise mean velocities for the CSM, the DSM, and no model in comparison with the particle-tracking velocimetry (PTV) data by Kasagi and Matsunaga (1995). The lower figure in Fig. 2 shows the close-up of the upper figure in a reattachment region near a lower wall. Whereas the overall profiles of the CSM, the DSM, and no model in the upper figure are almost the same, the lower figure shows that no model simulation gives under-predictions from $x/H = 4$ to $x/H = 8$ in a reattachment region near a lower wall. The CSM and DSM, however, agree well with the PTV data. The CSM gives a level of accuracy similar to the DSM in spite of a local model. The mean velocity profile of no model collapses with the other profiles everywhere except in the recirculation bubble. This is because the LES resolution turns out to be not a DNS but an adequately resolved LES in most of the domain. Even in this high resolution, the SGS viscosity affects the rms and Reynolds stress profiles as shown below.

Figs. 3 and 4 show the profiles of streamwise rms velocities and Reynolds shear stress for the CSM, the DSM, and no model in comparison with the PTV data by Kasagi and Matsunaga (1995). Whereas the profiles of the CSM, the DSM, and no model in Fig. 3 are almost the same, in

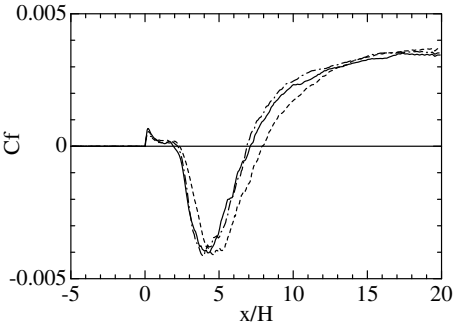

Fig. 7. Skin friction profiles. —, CSM; –·–, DSM; ----, no model.

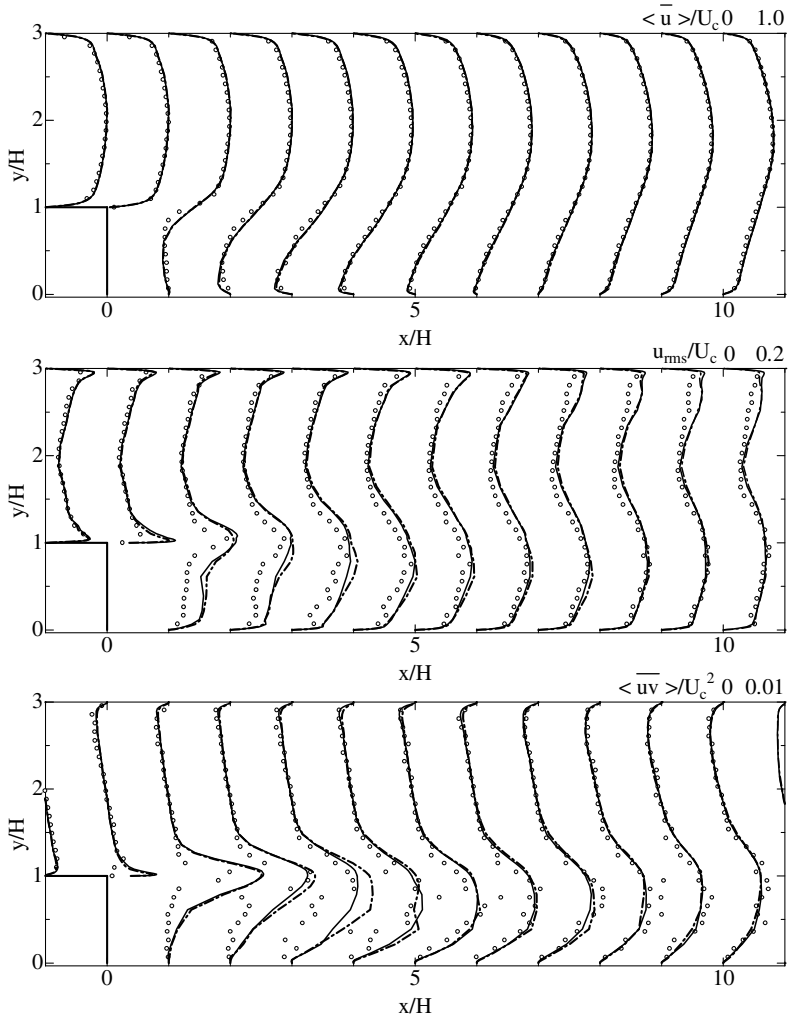

Fig. 6. Profiles of streamwise mean velocity, streamwise rms velocity, and Reynolds shear stress with a coarse mesh 134 × 56 × 60. —, CSM; –·–, DSM; ○, experimental data by Kasagi and Matsunaga (1995).

Fig. 4 no model simulation gives under-predictions from $x/H = 3$ to $x/H = 7$ at $y/H = 1$ in comparison with the CSM and DSM. The profile of the CSM agrees well with that of the DSM, although the CSM is a local SGS model.

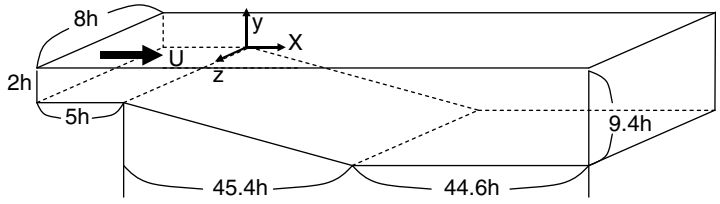

Fig. 8. Computational domain for an asymmetric plane diffuser.

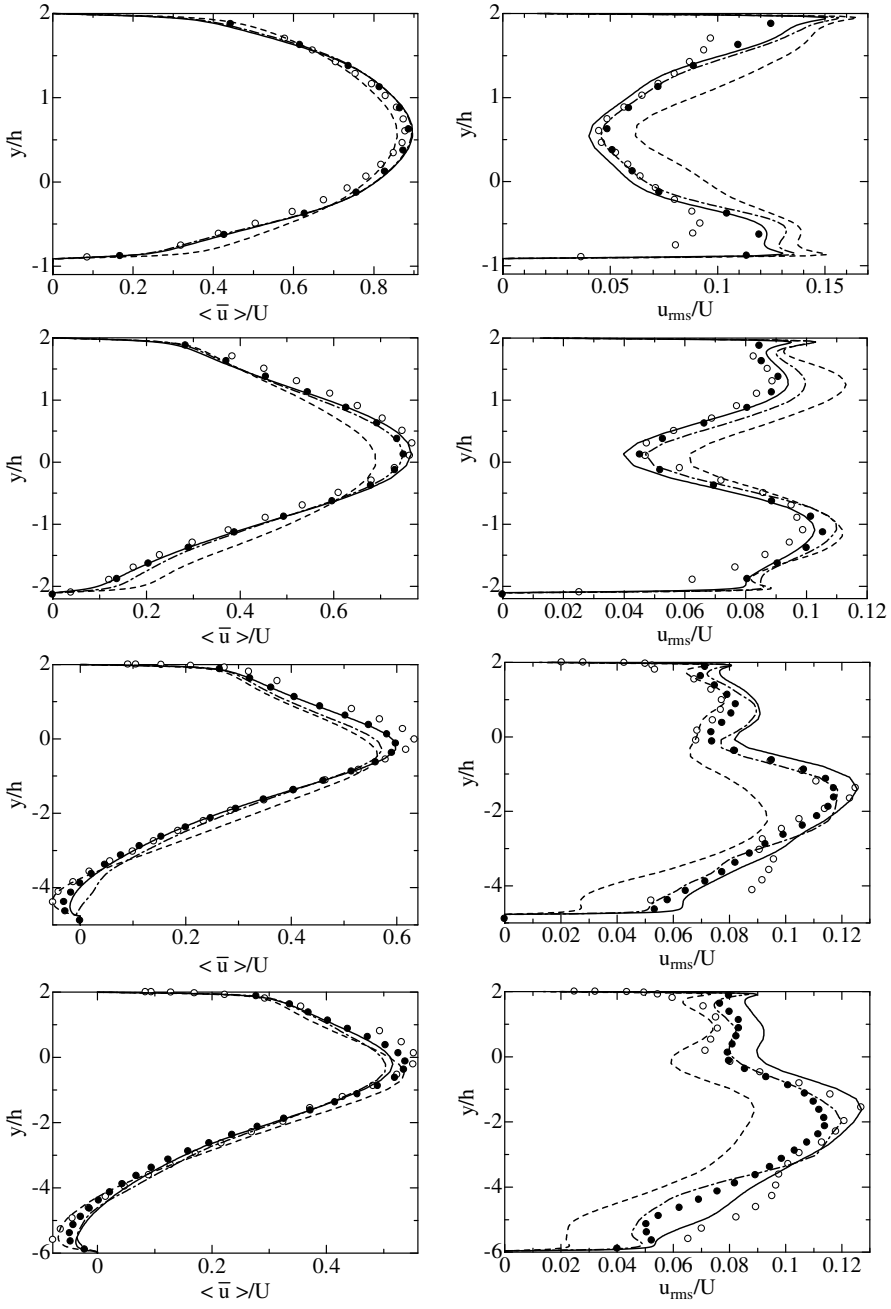

Fig. 9. Streamwise profiles of mean (left column) and rms (right column) velocities at $x/h = 5.18, 11.96, 27.1,$ and 33.86 from top to bottom. —, CSM; –·–, DSM; ----, no model; ●, fine DSM; ○, experimental data by Buice and Eaton (1997).

Fig. 5 shows the ratios of the SGS eddy viscosity ν_t and the molecular viscosity ν for the CSM and the DSM. The identical profiles of the mean velocity are caused by the small magnitude of the SGS viscosity and it is a characteristic of LES. The ratio for the CSM becomes small at $y/H = 1$ because the SGS eddy viscosity depends on $\overline{\Delta}_y$ in $\overline{\Delta} = (\overline{\Delta}_x\overline{\Delta}_y\overline{\Delta}_z)^{2/3}$, and the $\overline{\Delta}_y$ is stretched out to create the finest mesh. On the other hand, in the present study the ratio for the DSM does not depend on $\overline{\Delta}_y$ because the SGS eddy viscosity is determined using an average in homogeneous directions and not using a filtering for the y-direction (Germano et al., 1991, 1992). In the DSM the filtering in the y-direction is "optional", and in some studies the filtering is carried out. In that situation the DSM would give a similar profile at $y/H = 1$ to the CSM. Inagaki et al. (2002) showed the effect of y-direction filtering on eddy viscosity of DSM for a backward-facing step flow. Although the y-direction filtering causes large augmentations around $y/H = 0.5, 1.5$, the magnitude of eddy viscosity around $y/H = 1$ with y-direction filtering is almost the same as that without y-direction filtering. This is due to the dynamic procedure which models not C but $C\overline{\Delta}^2$.

However, the sharp profile of the CSM seems to be valid because in the small mesh the effect of ν_t to ν should be small. Although the SGS eddy viscosity of the CSM sharply changes at $y/H = 1$, the statistics of the first and second moments of the CSM were almost the same as those of the DSM. In addition, the CSM was numerically stable.

The CSM ran 15% faster in total CPU time than the DSM, which gives it a significant advantage over the DSM.

The profiles of streamwise mean velocity, streamwise rms velocity, and Reynolds shear stress with a coarse mesh $134 \times 56 \times 60$ are shown in Fig. 6. A uniform Δ_x is used to emphasize the performance of the CSM and DSM for the coarse mesh. Apparently, there are not so big difference between those two models except for the Reynolds stress profile at $x/H = 3$. The DSM shows somewhat overestimation.

Fig. 7 shows the skin friction profiles for the CSM, the DSM, and no model. The skin friction profiles of the CSM and DSM agree well, whereas that of no model gives a far reattachment point. The reattachment lengths for the CSM, DSM, and no model are 7.09, 6.87, and 7.88, respectively. However, an experimental result by Kasagi and Matsunaga (1995) was 6.51. A higher grid resolution of $384 \times 192 \times 64$ with the same stretch factors as the lower one was examined to confirm the reattachment length. In that study, the reattachment lengths for the CSM, DSM, and no model are 6.81, 6.75, and 7.13, respectively. For each resolution, it is confirmed that the CSM gives a similar prediction to the DSM.

3.2. Diffuser flow

Fig. 8 shows the computational domain for a turbulent flow through an asymmetric plane diffuser. The diffuser has a total expansion ratio of $4.7h$ and a single-sided deflection wall of 10°. An experiment for this configuration was carried out by Obi et al. (1993); more detailed experiments were conducted by Buice and Eaton (1997). Reynolds number based on the bulk velocity U, ν, and inlet height $2h$ is 18,000. The grid resolution is $400 \times 80 \times 80$ in the x, y, and z directions, respectively (x is the streamwise direction, y the one normal to the walls, z the spanwise one). The time step is $0.002h/U$, and statistics are obtained from averaging

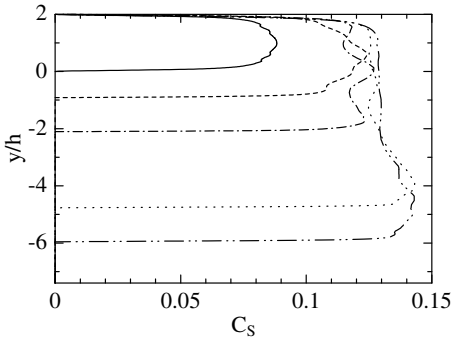

Fig. 10. Profiles of Smagorinsky constant $C_S = |C|^{1/2}$ for the CSM. —, $x/h = -5$; ----, 5.18; –·–, 11.96; ·····, 27.1; –··–, 33.86.

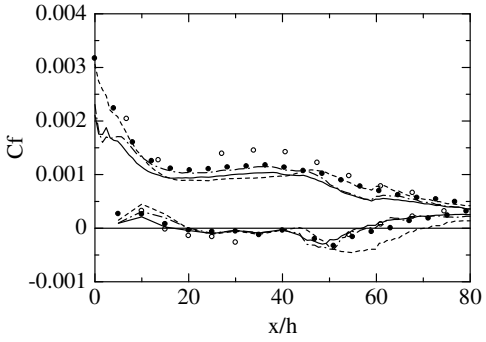

Fig. 11. Skin friction profiles. —, CSM; –·–, DSM; ----, no model; •, fine DSM; ○, experimental data by Buice and Eaton (1997).

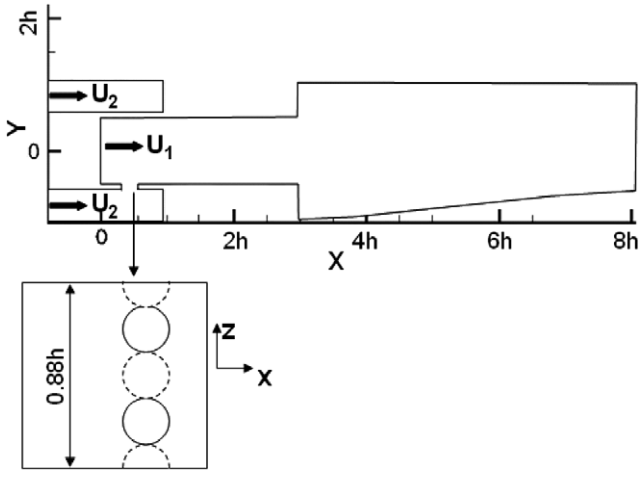

Fig. 12. Computational domain for staggered jets in crossflow.

over 40,000 time steps ($80h/U$ time units). An inflow condition is imposed at $x/h = -5$, and the unsteady inflow profile is given a fully developed channel flow at $Re_\tau = 500$. A convective condition is applied at the outflow boundary.

This simulation was carried out using an unstructured LES solver CDP, developed at the Center for Turbulence Research. Stanford University. For more information about the diffuser simulation, see Wu et al. (2006) and Schlüter et al. (2005). In this study, two times larger filter width was used for the CSM. Fig. 9 shows the streamwise profiles of mean (left column) and rms (right column) velocities at $x/h = 5.18, 11.96, 27.1$, and 33.86 from top to bottom for the CSM, the DSM, and no model. Those figures reflect the DSM results with a finer grid resolution ($590 \times 100 \times 110$) by Wu et al. (2006) and the experimental data by Buice and Eaton (1997). The CSM predicts almost the same streamwise mean velocity as the fine DSM at each x location. At $x/h = 27.1$ the DSM and no model underpredict the mean velocity profiles at $y/h = 0$, while the CSM agrees with the experimental data at $y/h = 0$. On the other hand, the CSM gives some over-predictions near an upper wall at $x/h = 27.1$ and 33.86 in comparison with the DSM and no model. Overall, the streamwise mean and rms velocities of the CSM agree well with those of the fine DSM and the experiment.

Fig. 10 shows the profiles of Smagorinsky constant $C_S = |C|^{1/2}$ for the CSM at each x location. At the centerline of the inlet, the C_S is about 0.09. As moving downstream, the C_S increases, and at the shear layer region of $x/h = 33.86$ the maximum C_S gives approximately 0.14, which is close to a well-known value 0.15 in a mixing layer.

Fig. 11 shows the skin friction profiles for the CSM, DSM, no model, fine DSM, and experimental data. The CSM under-predicts the skin friction from the inlet to $x/h = 40$ on an upper wall in comparison with the DSM and fine DSM, while the CSM gives a good prediction of the skin friction on a lower wall. Overall, the CSM predicts the skin friction similar to the DSM.

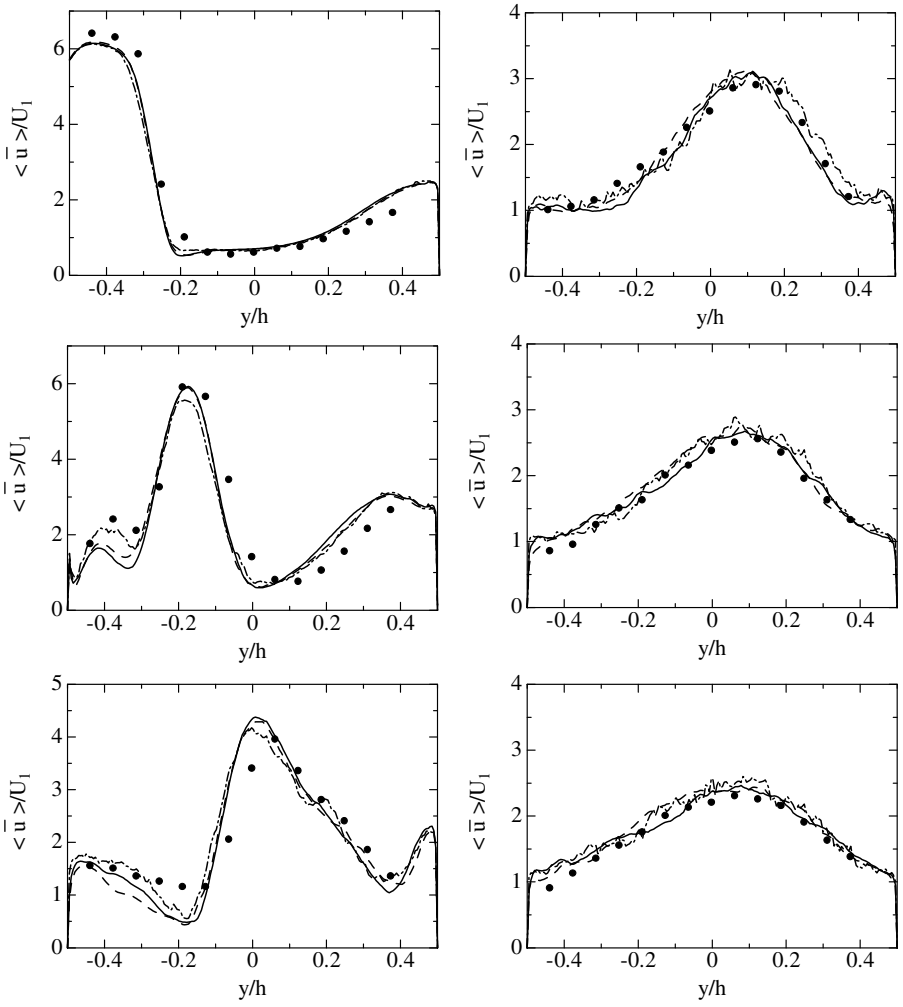

Fig. 13. Profiles of mean velocity ($\langle \bar{u} \rangle = (\langle \bar{u}_i \rangle^2)^{1/2}$) at $x = 0.45h$, $0.59h$, and $0.84h$ on the left column and $1.35h$, $1.60h$, and $1.86h$ on the right column from top to bottom. —, CSM; ----, LDSM; –·–, no model; ●, experimental data of mean velocity (CTR, 2007).

3.3. Staggered jets in crossflow

Fig. 12 shows the computational domain for staggered jets in crossflow. Liscinsky et al. (1992, 1993, 2006, 1999) carried out a series of the experiments. The upper figure shows the cross section view in the x–y-plane. There are three inlets of flow: upper, lower and center inlets. The inlet velocity of the center inlet is $U_1 = 1.0$ and that of the upper and lower inlets is $U_2 = 0.77$, respectively. The Reynolds number based on the center inlet velocity U_1, the height of the center inlet h, and the kinematic viscosity v is 40,500. About 2 million control volumes are used in the present simulation. Time step is determined by the CFL condition which equals 1, and statistics are obtained from averaging over 10,000 steps. One-dimensional results in Figs. 13–17 are obtained from the average at $z = -0.22h$ and $z = 0.22h$. An inflow condition with a laminar profile is imposed at $x = 0$ and $x = -0.79h$. A convective condition is applied at the outflow boundary.

The lower figure shows the cross section view of the staggered jets in x–z-plane. The solid and the dashed circles show the inlet of the jet from the lower inflow and the upper inflow, respectively. Namely, the upper and lower jets are arrayed as a staggered arrangement in the z-direction. The diameter of the inlet of jet is $0.22h$, and the width of this channel is $0.88h$. A periodic boundary condition is imposed in the z-direction. Even though the periodic boundary condition is used, the staggered jets make this flow field inhomogeneous in the z-direction.

Therefore, the dynamic model is adopted for the LDSM (Ghosal et al., 1995) because there is no homogeneous direction in this configuration. In this simulation, around 30% clipping of total control volumes was conducted for the LDSM.

Figs. 13 and 14 show the profiles of the mean velocity and the intensity of whole velocity fluctuation ($\langle\bar{u}\rangle = (\langle\bar{u}_i\rangle^2)^{1/2}$ and $u_{\mathrm{rms}} = (\langle\bar{u}_i - \langle\bar{u}_i\rangle\rangle^2)^{1/2}$) at $x = 0.45h$, $0.59h$, $0.84h$, $1.35h$, $1.60h$, and $1.86h$ for the CSM, the LDSM and no model. In Fig. 13, the dots show the experimental data of mean velocity (CTR, 2007), which were obtained from the United Technologies Research Center. The mean velocity profiles of the CSM and LDSM show good

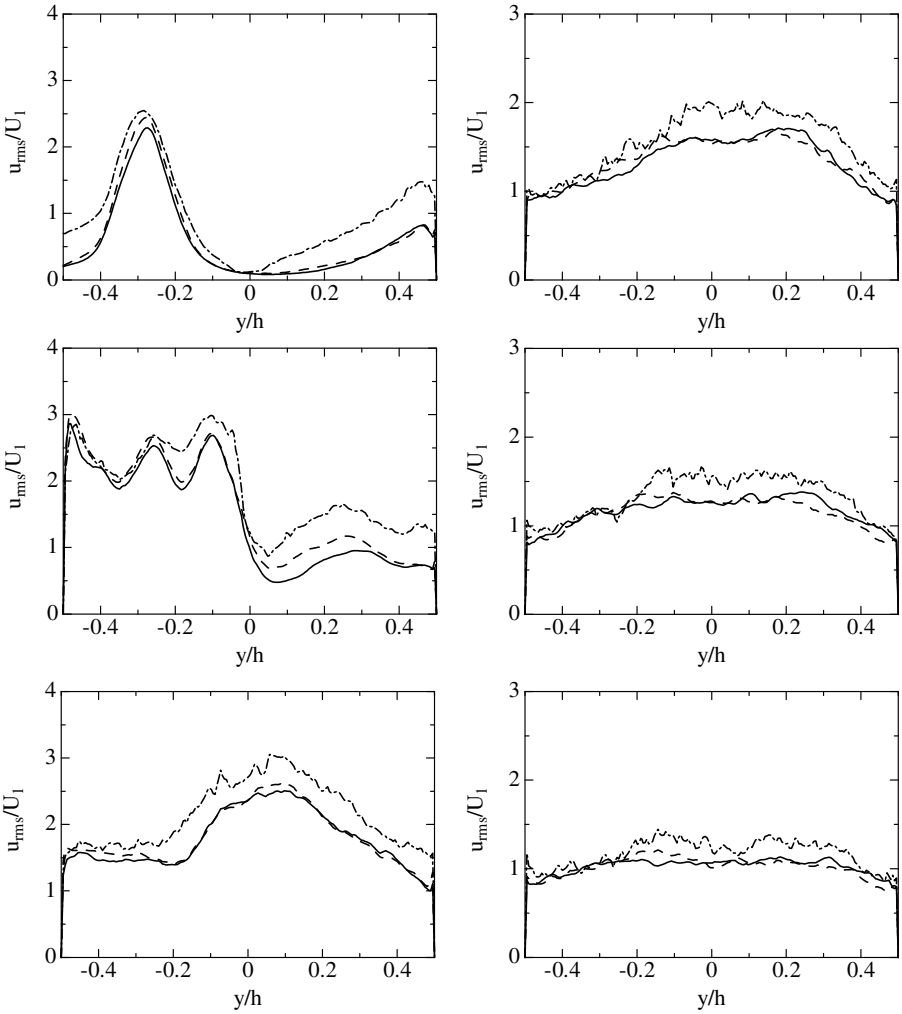

Fig. 14. Profiles of the intensity of whole velocity fluctuation ($u_{\mathrm{rms}} = (\langle\bar{u}_i - \langle\bar{u}_i\rangle\rangle^2)^{1/2}$) at $x = 0.45h$, $0.59h$, and $0.84h$ on the left column and $1.35h$, $1.60h$, and $1.86h$ on the right column from top to bottom. —, CSM; ----, LDSM; –·–, no model.

agreement with those of experimental data. The mean velocity profiles of the CSM and LDSM show good agreement. In addition, the mean velocity and intensity of whole velocity fluctuation of the CSM agree well with those of LDSM. No model, however, gives higher intensity than the CSM and LDSM because no model contains the fluctuation of high wave number which should be transferred to the SGS energy. It leads to a low mean velocity as seen at $y = -0.2h$ in $x = 0.59h$ plane.

Fig. 15 shows the ratios of the SGS eddy viscosity and the molecular viscosity at $x = 0.45h$, $0.59h$, $0.84h$, $1.35h$, $1.60h$, and $1.86h$ for the CSM and the LDSM. Those profiles of the CSM are similar to those of the LDSM. In $x = 0.45h$ and $0.59h$, the CSM gives higher value than the LDSM. On the other hand, in $x = 0.84h$, $1.35h$, $1.60h$, and $1.86h$, the LDSM predicts higher value than the CSM.

Fig. 16 shows the profiles of Smagorinsky constant $C_S = |C|^{1/2}$ at $x = 0.45h$, $0.59h$, $0.84h$, $1.35h$, $1.60h$, and $1.86h$ for the CSM and the LDSM. At $y = 0$ in $x = 0.45h$, the CSM gives higher value than the LDSM, but there seems to be almost a laminar flow because the shear of the mean velocity and the intensity of whole velocity fluctuation are nearly zero as shown in Figs. 13 and 14. Although the SGS viscosity of the CSM exhibits a peak at $y = 0$ in Fig. 15, the traceless SGS stress tensor $\tau^a_{ij} = -2\nu_T\overline{S}_{ij}$ becomes nearly zero.

Fig. 17 shows the profiles of the model parameter C for the LDSM before clipping at $x = 0.45h$ and $0.59h$. The model parameter C takes negative values, so that those negative values are clipped as zero in a practical procedure. This affects the SGS eddy viscosity, and it gives the deference of its profiles between the CSM and LDSM near the wall.

Fig. 18 shows the distribution of passive scalar ϕ for the CSM. The passive scalar of $\phi = 1$ is injected from the upper and lower inlets. The lower figure shows the zoom view near a jet inlet. Some eddies based on the Kelvin–Helmholtz (K–H) instability are induced along the jet, so that the mixing of the jet is effectively promoted. The K–H eddies are visualized in Fig. 19 with the second invariant

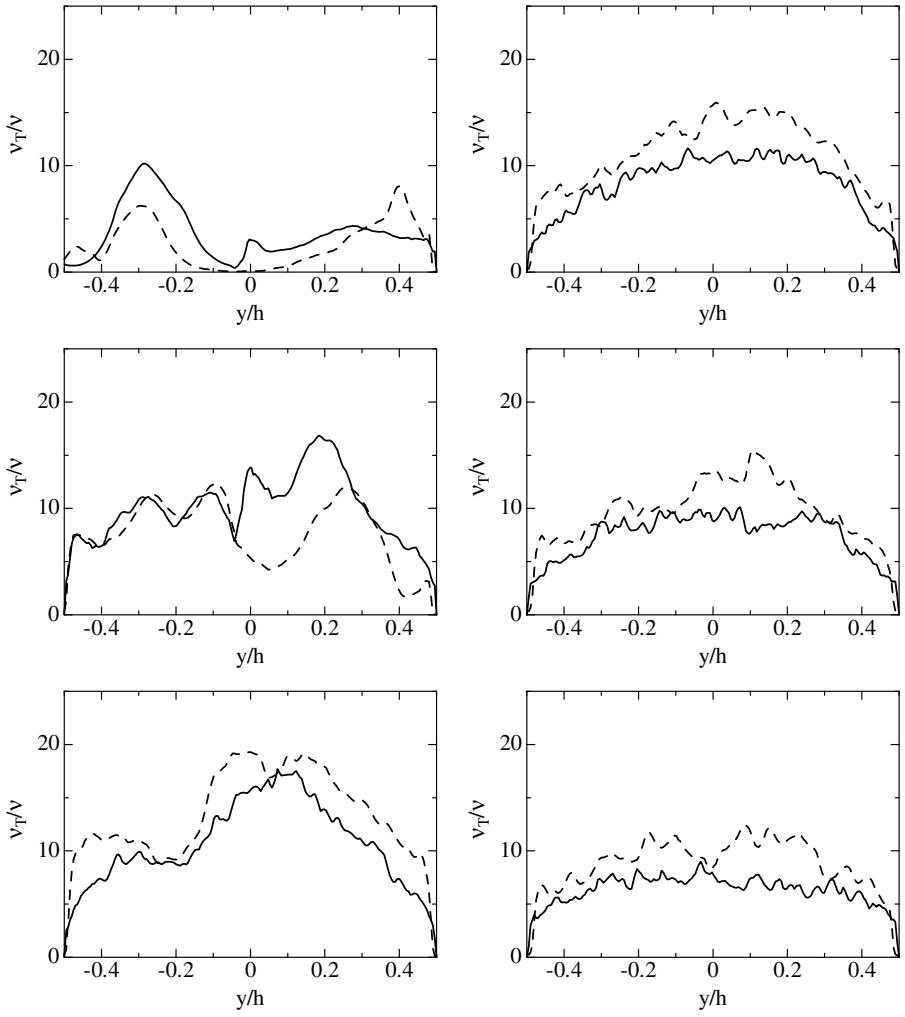

Fig. 15. Ratios of the SGS eddy viscosity and the molecular viscosity at $x = 0.45h$, $0.59h$, and $0.84h$ on the left column and $1.35h$, $1.60h$, and $1.86h$ on the right column from top to bottom. —, CSM; ----, LDSM.

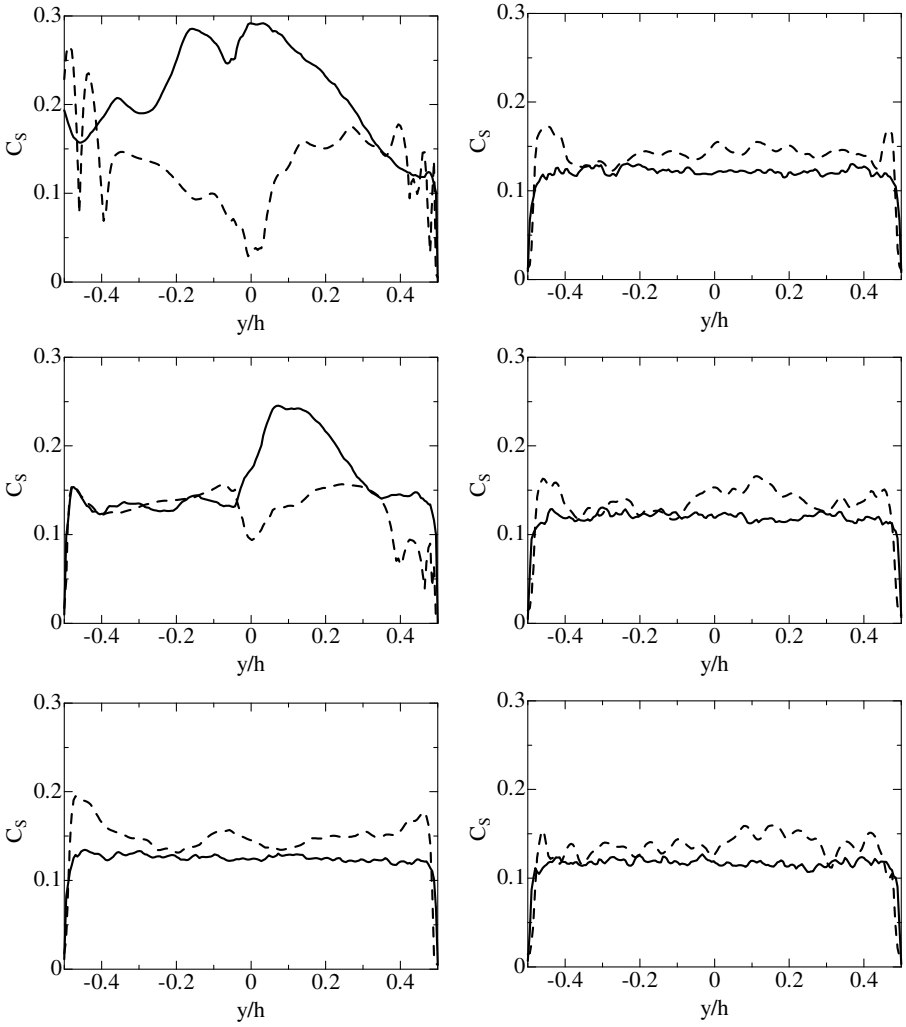

Fig. 16. Profiles of Smagorinsky constant $C_S = |C|^{1/2}$ at $x = 0.45h$, $0.59h$, and $0.84h$ on the left column and $1.35h$, $1.60h$, and $1.86h$ on the right column from top to bottom. —, CSM; ----, LDSM.

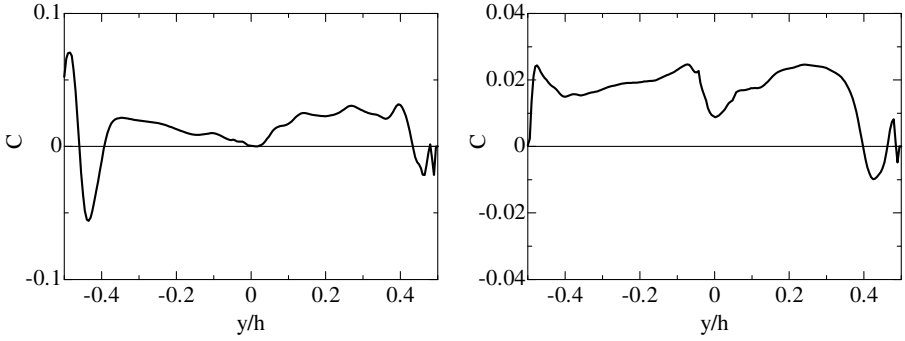

Fig. 17. Profiles of the model parameter C for the LDSM before clipping at $x = 0.45h$ (left) and $0.59h$ (right).

$Q = 100$ of red (light gray). The blue (dark gray) in the figure depicts the iso-surface of $Q = -100$ which shows high strain regions. The high strain regions are distribute near the K–H eddies. This means that the negative second invariant is a good marker to obtain the high strain region which gives the high SGS eddy viscosity.

4. Conclusions

A local SGS model based on coherent structures has been applied to complex geometries: a backward-facing step flow, asymmetric plane diffuser, staggered jets in cross-flow. A structured code was used for the backstep flow, and

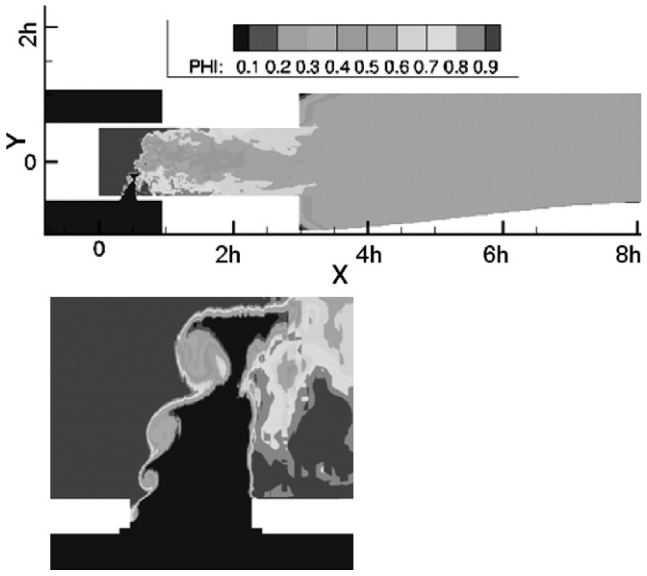

Fig. 18. Distribution of passive scalar ϕ for the CSM.

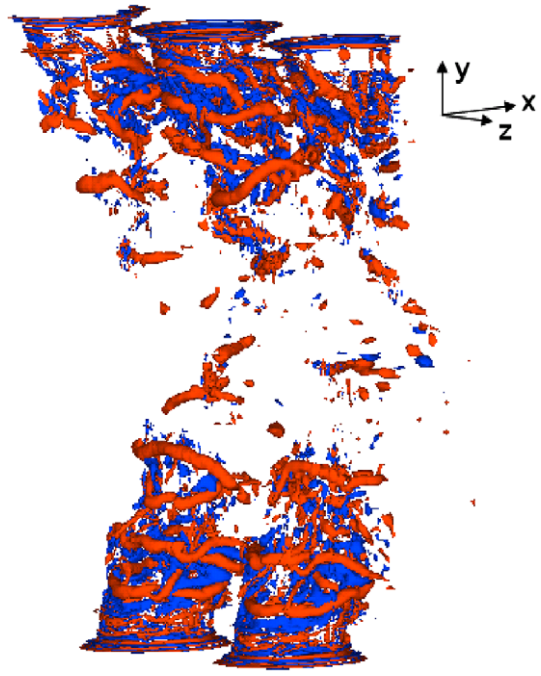

Fig. 19. Distribution of the second invariant near the jet inlets. Red (light gray), $Q = 100$; blue (dark gray), $Q = -100$; $-2827 \leqslant Q \leqslant 9799$. (For interpretation of the references to colour in this figure legend, the reader is referred to the web version of this article.)

an unstructured one was adopted for the diffuser flow and staggered jets, respectively. For all configurations, the local coherent structure model gives almost the same performance as the dynamic Smagorinsky model using an average in homogeneous directions and the dynamic localization model. The coherent structure model is inexpensive and efficient in comparison with the dynamic model, and is numerically stable without averaging. The present model will be suitable for the complex geometry without any homogeneous directions.

Recently, Park et al. (2006) proposed a dynamic SGS eddy viscosity model with a global model coefficient in the Vreman model (Vreman, 2004). A dynamic procedure to determine the model coefficient is proposed based on the "global equilibrium" between the SGS dissipation and the viscous dissipation. The model coefficient determined is globally constant in space but varies only in time. A posteriori tests of the proposed dynamic model are conducted in forced isotropic turbulence, turbulent channel flows, flow over a circular cylinder, and flows over a sphere; excellent performance for all flows is obtained. This procedure is robust and readily applied to complex flows without homogeneous directions. This dynamic procedure would be applicable to the present local SGS model, but its application is remained in the future study.

Acknowledgements

HK is deeply grateful to Professor Parviz Moin for providing the research opportunity as a senior visiting fellow at the Center for Turbulence Research, Stanford University. Parts of this work were done there during his stay. HK would like to thank Dr. Donghyun You for his valuable comments and for improving parts of the presentation of this manuscript, Professor Gianluca Iaccarino for providing some references of the staggered jets in crossflow, Dr. James D. Holdeman for sending me a lot of information of the experiments of the staggered jets in crossflow, and Dr. David S. Liscinsky for permitting to use the experimental data of the staggered jets in crossflow.

References

Akselvoll, K., Moin, P., 1995. Large eddy simulation of turbulent confined coannualar jets and turbulent flow over a backward facing step. Report TF-63. Thermosciences Division, Departmnet of Mechnical Engineering, Stanford University.

Blomeyer, M., Krautkremer, B., Hennecke, D.K., Doerr, 1999. Mixing zone optimization of a rich-burn/quick-mix/lean-burn combustor. J. Propulsion Power 15, 288–295.

Buice, C.U., Eaton, J.K., 1997. Experimental investigation of flow through an asymmetric plane diffuser. Ph.D. thesis, Stanford University.

Chakraborty, P., Balachandar, S., Adrian, R.J., 2005. On the relationships between local vortex identification schemes. J. Fluid Mech. 535, 189–214.

Chong, M.S., Perry, A.E., Cantwell, B.J., 1990. A general classification of three-dimensional flow fields. Phys. Fluids A 2, 765–777.

Center for Turbulence Research, Stanford University, 2007. Private communication.

Da Silva, C.B., Métais, O., 2002. On the influence of coherent structures upon interscale interactions in turbulent plane jets. J. Fluid Mech. 473, 103–145.

Germano, M., Piomelli, U., Moin, P., Cabot, W.H., 1991. A dynamic subgrid-scale eddy viscosity model. Phys. Fluids A 3, 1760–1765.

Ghosal, S., Lund, T.S., Moin, P., Akselvoll, K., 1995. A dynamic localization model for large-eddy simulation of turbulent flows. J. Fluid Mech. 286, 229–255.

Ham, F., Iaccarino, G., 2004. Energy conservation in collocated discretization schemes on unstructured meshes. In: Annual Research Briefs – 2004. Center for Turbulence Research, Stanford, pp. 3–14.

Holdeman, J.D., Clisset, J.R., Moder, J.P., Lear, W.E., 2006. On the Mixing of Single and Opposed Rows of Jets With a Confined Crossflow, pp. 1–217 (NASA/TM-2006-214226).

Hunt, J.C.R., Wray, A.A., Moin, P., 1988. Eddies, streams, and convergence zones in turbulent flows. In: Center for Turbulence Research Report. Center for Turbulence Research, Stanford, pp. 193–208.

Inagaki, M., Kondoh, T., Nagano, Y., 2002. A mixed-time-scale SGS model with fixed model-parameters for practical LES. In: Rodi, W., Fueyo, N. (Eds.), Engineering Turbulence Modelling and Experiments, vol. 5. Elsevier, pp. 257–266.

Jeong, J., Hussain, F., 1995. On the identification of a vortex. J. Fluid Mech. 285, 69–94.

Jiménez, J., Wray, A.A., Saffman, P.G., Rogallo, R.S., 1993. The structure of intense vorticity in isotropic turbulence. J. Fluid Mech. 255, 65–90.

Kasagi, N., Matsunaga, A., 1995. Three-dimensional particle-tracking velocimetry measurement of turbulences statistics and energy budget in a backward-facing step flow. Int. J. Heat Fluid Flow 16, 477–485.

Kida, S., Ohkitani, K., 1992. Spatiotemporal intermittency and instability of a forced turbulence. Phys. Fluids A 4, 1018–1027.

Kobayashi, H., 2005. The subgrid-scale models based on coherent structures for rotating homogeneous turbulence and turbulent channel flow. Phys. Fluids 17, 045104.

Kobayashi, H., 2006. Large eddy simulation of magnetohydrodynamic turbulent channel flows with local subgrid-scale model based on coherent structures. Phys. Fluids 18, 045107.

Kobayashi, H., 2008. Large eddy simulation of magnetohydrodynamic turbulent duct flows. Phys. Fluids 20, 015102.

Lesieur, M., Métais, O., 1996. New trends in large-eddy simulations of turbulence. Annu. Rev. Fluid Mech. 28, 45–82.

Lilly, D.K., 1992. A proposed modification of the germano subgrid-scale closure method. Phys. Fluids A 4, 633–635.

Liscinsky, D.S., True, B., Vranos, A., Holdeman, J.D., 1992. Experimental study of cross-stream mixing in a rectangular duct. AIAA paper 92-3090/NASA-TM-105694, pp. 1–11.

Liscinsky, D.S., Vranos, A., Lohmann, R.P., 1993. Experimental study of cross flow mixing in cylindrical and rectangular ducts. NASA-CR-187141, pp. 1–51.

Mahesh, K., Constantinescu, G., Moin, P., 2004. A numerical method for large-eddy simulation in complex geometries. J. Comput. Phys. 197, 215–240.

Meneveau, C., Lund, T.S., Cabot, W.H., 1996. A lagrangian dynamic subgrid-scale model of turbulence. J. Fluid Mech. 319, 353–385.

Miyauchi, T., Tanahashi, M., 2001. Coherent fine scale structure in turbulence. In: T. Kambe et al. (Eds.), IUTAM Symposium on Geometry and Statistics of Turbulence. Kluwer, pp. 67–76.

Natrajan, V.K., Christensen, K.T., 2006. The role of coherent structures in subgrid-scale energy transfer within the log layer of wall turbulence. Phys. Fluids 18, 065104.

Nicoud, F., Ducros, F., 1999. Subgrid-scale stress modelling based on the square of the velocity gradient tensor. Flow, Turbulence Combust. 62, 183–200.

Obi, S., Aoki, K., Masuda, S., 1993. Experimental and computational study of turbulent separating flow in an asymmetric plane diffuser. In: Ninth Symposium on Turbulent Shear Flows, Kyoto, pp. 16–19.

Park, N., Lee, S., Lee, J., Choi, H., 2006. A dynamic subgrid-scale eddy viscosity model with a global model coefficient. Phys. Fluids 18, 125109.

Pierce, C.D., 2001. Progress-variable approach for large-eddy simulation of turbulent combustion. Ph.D. thesis, Stanford University.

Rogallo, R.S., Moin, P., 1984. Numerical simulation of turbulent flows. Annu. Rev. Fluid Mech. 16, 99–137.

Salvetti, M.V., Banerjee, S., 1995. A priori tests of a new dynamic subgrid-scale model for finite-difference large-eddy simulations. Phys. Fluids 7, 2831–2847.

Schlüter, J., Wu, X., Pitsch, H., 2005. Large-eddy simulation of a separated plane diffuser. AIAA paper (AIAA 2005-0672), January 2005.

Shimomura, Y., 1994. Subgrid-scale algebraic stress model of turbulence. J. Phys. Soc. Jpn. 63, 5–9.

Shimomura, Y., 1995. Performance of the subgrid-scale algebraic stress model in large eddy simulation. In: Daiguji, H., Miyake, Y. (Eds.), Mathematical Modelling of Turbulent Flows, Proceedings of the International Symposium on Mathematical Modelling of Turbulent Flows. Japan Society of Computational Fluid Dynamics, pp. 321–327.

Smagorinsky, J., 1963. General circulation experiments with the primitive equations. I. The basic experiment. Month. Weather Rev. 91, 99–152.

Tanahashi, M., Miyauchi, T., Yoshida, T., 1996. Characteristics of small scale vortices related to turbulent energy dissipation. In: Winoto, S.H., Chew, Y.T., Wijeysundera, N.E. Transport Phenomena in Thermal-Fluids Engineering, Proceedings of the Ninth International Symposium on Transport Phenomena in Thermal-Fluids Engineering, vol. II. Pacific Centre of Thermal-Fluids Engineering, Singapore, pp. 1256–1261.

Tanahashi, M., Miyauchi, T., Matsuoka, K., 1997. Coherent fine scale structures in temporally developing turbulent mixing layers. In: Hanjalić, K., Peeters, T.W.J. (Eds.), Turbulence, Heat and Mass Transfer, Proceedings of the Second International Symposium on Turbulence, Heat and Mass Transfer, vol. 2. Delft University Press, Netherlands, pp. 461–470.

Vincent, A., Meneguzzi, M., 1991. The spatial structure and statistical properties of homogeneous turbulence. J. Fluid Mech. 225, 1–20.

Vreman, A.W., 2004. An eddy-viscosity subgrid-scale model for turbulent shear flow: Algebraic theory and applications. Phys. Fluids 16, 3670–3681.

Wu, X., Schlüter, J., Moin, P., Pitsch, H., Iaccarino, G., Ham, F., 2006. Computational study on the internal layer in a diffuser. J. Fluid Mech. 550, 391–412.

Yoshizawa, A., Kobayashi, K., Kobayashi, T., Taniguchi, N., 2000. The A nonequilibrium fixed-parameter subgrid-scale model obeying the near-wall asymptotic constraint. Phys. Fluids 12, 2338–2344.

Zhou, J., Adrian, R.J., Balachandar, S., Kendall, T.M., 1999. Mechanisms for generating coherent packets of hairpin vortices. J. Fluid Mech. 387, 353–396.